

Neuromorphic Visual Scene Understanding with Resonator Networks

Alpha Renner,^{1,*} Lazar Supic,² Andreea Danielescu,² Giacomo Indiveri,¹ Bruno A. Olshausen,³ Yulia Sandamirskaya,⁴ Friedrich T. Sommer,^{3,4,†} and E. Paxon Frady^{4,‡}

¹*Institute of Neuroinformatics, University of Zurich and ETH Zurich, Switzerland*

²*Accenture Labs, San Francisco*

³*Redwood Center for Theoretical Neuroscience, UC Berkeley*

⁴*Intel Neuromorphic Computing Lab*

Understanding a visual scene by inferring identities and poses of its individual objects is still and open problem. Here we propose a neuromorphic solution that utilizes an efficient factorization network based on three key concepts: (1) a computational framework based on Vector Symbolic Architectures (VSA) with complex-valued vectors; (2) the design of Hierarchical Resonator Networks (HRN) to deal with the non-commutative nature of translation and rotation in visual scenes, when both are used in combination; (3) the design of a multi-compartment spiking phasor neuron model for implementing complex-valued resonator networks on neuromorphic hardware. The VSA framework uses vector binding operations to produce generative image models in which binding acts as the equivariant operation for geometric transformations. A scene can therefore be described as a sum of vector products, which in turn can be efficiently factorized by a resonator network to infer objects and their poses. The HRN enables the definition of a partitioned architecture in which vector binding is equivariant for horizontal and vertical translation within one partition and for rotation and scaling within the other partition. The spiking neuron model allows mapping the resonator network onto efficient and low-power neuromorphic hardware. Our approach is demonstrated on synthetic scenes composed of simple 2D shapes undergoing rigid geometric transformations and color changes. A companion paper demonstrates the same approach in real-world application scenarios for machine vision and robotics.

INTRODUCTION

Visual scene understanding is a long-standing problem of machine vision and artificial intelligence. It is a notoriously hard –and largely unsolved– computational problem, as it requires searching over a very large space of possible configurations for how objects may be combined along with variations in pose, color, lighting, and other features [1, 2]. Convolutional artificial neural networks have been proposed as a possible approach to solving this problem. However, this approach typically requires large amounts of training data as well as additional augmentations of the data to handle variations in pose or style. Furthermore, even with these training expedients, their performance is often brittle [3, 4] and easily fooled by both artificial and real-world imagery [5, 6]. Of more concern from an engineering and security standpoint is the fact that their operation is opaque because the factors of variation in visual scenes are entangled in complicated ways via their typically large number of parameters. This makes it difficult to trace information flow and understand the system sufficiently well to fix the failure modes.

It has long been proposed that the brain solves the visual scene understanding problem via “analysis by synthesis” whereby a generative model, which holds knowledge of scene components and their transformations, is used to infer the components of a scene based on how well their configurations explain the image data [7–9]. However, inference in these models can require many iterations to converge, and the high computational cost associated with these operations has prevented their widespread deployment. Recent work has shown that for workloads that require recurrent iterative computations, *neuromorphic computing* can vastly outperform CPU and GPU-based approaches [10]. Specifically, custom spike-based neuromorphic chips [10–14] accelerate computing times and reduce power consumption figures thanks to their parallelism, in-memory processing [15], sparsity, and event-based [16] nature. To leverage this advantage of neuromorphic hardware for scene understanding, we use a programming framework that offers an explicit binding operation, thus overcoming the so-called feature binding problem in conventional artificial neural networks [17–19]. For example, in convolutional networks, processing the image through a cascade of linear filtering, thresholding, and pooling operations discards the binding between features, objects, and their transformations. This results in representations that are sufficient to pass certain classification benchmarks but which are easily confused when tested more rigorously, e.g., [20].

* alpren@ini.uzh.ch

† fsommer@berkeley.edu

‡ e.paxon.frady@intel.com

Our neuromorphic approach to scene analysis is based on a programming framework stemming from Cognitive Science that represents symbols or variables as high-dimensional vectors and then computes on these representations via an explicit algebra consisting of addition, multiplication, and permutation [21–23]. Models of this type are now referred to as Vector Symbolic Architectures (VSAs) [24], or Hyperdimensional Computing (HC) [25], and they have been proposed as a powerful algorithmic framework for emerging computing fabrics that exhibit non-deterministic behavior at small scales and low power [26]. Here, we leverage recent developments in VSA and HC for designing a neuromorphic algorithm for scene analysis: 1) a mathematical framework that extends VSAs to represent continuous variables and functions [27], and 2) a *resonator network* that efficiently solves multi-factor vector factorization in VSAs [28, 29]. The first development enables us to encode an image in a VSA representation such that binding (vector multiplication) acts as the equivariant operation for specific geometric transformations [27], while the second one makes it tractable to infer objects and their transformations via vector factorization [28, 29].

The approach proposed falls within the larger family of multilinear models for inferring object shapes and their transformations in the context of a generative image model. These include early proposals by Pitts & McCulloch (1947)[30] and Hinton (1981)[31] for remapping sensory information into a canonical reference frame, neurobiological models such as dynamic routing [32], map-seeking circuits [33, 34], as well as bilinear models that learn to disentangle form vs. motion (or ‘style’ vs. ‘content’) [35–39]. In the particular case of bilinear models, the generative network is mathematically formulated as a tensor product. This tensor operation is, in fact, closely related to the VSA binding operation used here [40].

The paper is organized as follows. First, we describe how an image can be encoded in a VSA representation so that the binding operation is the equivariant operation for translation. With the same encoding scheme, we then formulate a generative model of a scene composed of translated template shapes and show how resonator networks [28] can infer translations and object templates that generated a given image. Extending this approach, we develop an algorithm for analyzing scenes composed of arbitrary rigid transforms of shape templates. The algorithm is based on a resonator network with a novel architecture, the *hierarchical resonator network*. Finally, we demonstrate how to implement the essential components of the hierarchical resonator network on Intel’s neuromorphic research chip, Loihi [41], utilizing an efficient spike-timing code.

REPRESENTING IMAGES IN HYPERVECTORS

High-dimensional random vectors with independent identically distributed (i.i.d.) components are approximately orthogonal, that is, pairs of vectors are very likely to have a small inner product. VSAs leverage this separation by representing individual symbols by i.i.d. random vectors (\mathbf{a} , \mathbf{b} , etc.) in an N -dimensional space [21, 25]. Recently, VSAs have been generalized to Vector Function Architectures (VFAs) [27] that can represent not only discrete symbols but also functions [27] and real-valued quantities [42, 43]. VSAs and VFAs typically offer two complementary dyadic vector operations to form composite data structures, superposition and binding/unbinding, which preserve the vector dimension. The N -dimensional vectors representing atomic and composite data structures during a computation are called *hypervectors*. During computation, the execution of vector operations is interleaved with parsing/decoding and error correction, exploiting similarity-based access of the interpretable hypervectors stored in the so-called *codebook*, for example, through nearest-neighbor search or auto-associative content-addressable memory [44, 45].

Here we use Fourier Holographic Reduced Representations (FHRR) [21, 46], a VSA whose atomic hypervectors are composed of phasors, i.e., complex-valued variables with unit amplitude. Similarity between two FHRR hypervectors is measured by the real part of the normalized inner product, $\frac{1}{N}\Re(\mathbf{a}^\dagger \mathbf{b})$, where \mathbf{a}^\dagger is the complex conjugate vector transpose. The binding operation in FHRR is the Hadamard product or component-wise multiplication \odot , with $\mathbf{a} \odot \mathbf{b}$ for *binding*, and $\mathbf{a} \odot \mathbf{b}^*$ for *unbinding*, where \mathbf{b}^* is the complex conjugate. The *superposition* operation is vector summation, $\mathbf{a} + \mathbf{b}$.

To encode an image as a hypervector, VFA index vectors are created to encode pixel location. We choose two fixed complex-valued FHRR vectors \mathbf{h} (i.e. $h_j = e^{i\phi_j}$, $\phi_j \sim \mathcal{U}[0, 2\pi]$, with $\mathcal{U}[0, 2\pi]$ the uniform distribution), and \mathbf{v} . A pixel at the Cartesian image coordinates x and y is represented by the index vector $\mathbf{h}^x \odot \mathbf{v}^y$. Note that the complex exponential is multi-valued, i.e. $(e^{i\phi_j})^x = e^{x(i\phi_j + 2\pi n)} \forall n \in \mathbb{Z}$, but we define the operation as returning only the principal value with $n = 0$.

Following [27], the image $Im(x, y)$ is encoded as a function over the pixel space via the superposition of index vectors weighted by their corresponding image pixel values $\mathbf{s} = \sum_{x,y} Im(x, y) \cdot \mathbf{h}^x \odot \mathbf{v}^y$. This encoding is similar to the Discrete Fourier transform but with frequencies chosen randomly and not with regular spacing [47]. Interestingly, important features of the Fourier transform, such as the convolution theorem, remain valid even with the frequencies randomized. Further, we form a codebook with random vectors for indexing the color channels red, green and blue,

$\mathbf{G} = [\mathbf{r}, \mathbf{g}, \mathbf{b}] \in \mathbb{C}^{N \times 3}$. The hypervector representation of a color image is then given as:

$$\mathbf{s} = \sum_{x,y,c} \text{Im}(x, y, c) \cdot \mathbf{G}_c \odot \mathbf{h}^x \odot \mathbf{v}^y =: \Phi \mathbf{I}. \quad (1)$$

where \mathbf{G}_c indicates the vector from the codebook that corresponds to the color channel. The definition on the right of (1) makes it explicit that hypervector encoding is linear, with $\mathbf{I} \in \mathbb{R}^{(3P_x P_y)}$ the image reshaped as a vector, and $\Phi \in \mathbb{C}^{N \times (3P_x P_y)}$ the codebook matrix of hypervectors for each index configuration $\{x, y, c\}$. Conversely, decoding the image from the hypervector uses the conjugate transpose as the linear transform, $\mathbf{I} = \frac{1}{N} \Re(\Phi^\dagger \mathbf{s})$. Since the codebook entries are only approximately orthogonal, decoding introduces small amounts of noise in the image reconstruction, which can be quantified and mitigated [48]. In this context, these noise effects are minimal.

Image encoding with (1) has pivotal properties for enabling scene factorization. Most importantly, it ensures that the *equivariant vector operation* for image translation is the binding operation, i.e. $\mathbf{s} \odot \mathbf{h}^{\Delta x} \odot \mathbf{v}^{\Delta y}$, which is the VFA representation of the image translated by $\Delta x, \Delta y$, since

$$\mathbf{s} \odot \mathbf{h}^{\Delta x} \odot \mathbf{v}^{\Delta y} = \sum_{x,y} \text{Im}(x, y) \cdot \mathbf{h}^{x+\Delta x} \odot \mathbf{v}^{y+\Delta y} = \sum_{x,y} \text{Im}(x - \Delta x, y - \Delta y) \cdot \mathbf{h}^x \odot \mathbf{v}^y. \quad (2)$$

Also, note that image translation is well-defined for continuous values of $\Delta x, \Delta y$, allowing the recognition of shapes shifted by fractions of a pixel.

A GENERATIVE MODEL OF SCENES USING VSA VECTOR OPERATIONS

To demonstrate scene factorization, we focus on synthetic images of simple visual scenes composed of object templates, in our case letters, that are translated and given one of 7 colors. Multiple objects are independently generated and then added to the scene. The image understanding task is to extract from an input image the identities, colors, and locations of the objects.

We use the VFA framework to build a generative model for such simple synthetic images. The set of letter templates forms a matrix $\mathbf{P} \in \mathbb{R}^{(P_x P_y) \times D}$, where $D = 26$ is the number of different templates. As in (1), templates of the letters can be encoded as hypervectors via

$$\mathbf{d}_a = \sum_{x,y} \mathbf{P}_a(x, y) \cdot \mathbf{h}^{x-\delta_x} \odot \mathbf{v}^{y-\delta_y}, \quad (3)$$

where δ_x, δ_y are offsets to center the pattern within its own object-centered reference frame (see Methods for discussion of template alignment). Each hypervector for the templates is stored in the matrix $\mathbf{D} = \Phi \mathbf{P}$, with Φ containing the vectors for each pixel as described in (3).

The equivariance property of vector binding can be used to color and position a template in the scene. Furthermore, vector superposition is employed for adding different objects into the image. All told, the VFA representation of a generated scene composed of L objects is:

$$\mathbf{s} = \sum_{i=1}^L \mathbf{d}_{p_i} \odot \mathbf{h}^{x_i} \odot \mathbf{v}^{y_i} \odot \mathbf{c}_{c_i}. \quad (4)$$

In the generative model based on (4), each factor of variation (p_i, x_i, y_i, c_i) is sampled uniformly. There are 7 colors used in the generative model given by a matrix $\mathbf{B} \in \mathbb{R}^{3 \times 7}$ with, for instance, $\mathbf{B}_{cyan} = [0, 1, 1]$. The VSA codebook for colors is $\mathbf{C} = \mathbf{G}\mathbf{B}$.

For an example of a hypervector produced by the generative VFA model (4), see Fig. 1A. For rendering the generated scene in pixel space, the hypervector can be decoded, as described earlier. To enable inference in the generative model (4), each generative factor has to be represented by sufficiently dissimilar hypervectors, even if the corresponding elements in the image domain are correlated, for example, shape templates with large overlap, like ‘‘c’’ versus ‘‘o’’.

Decorrelated hypervectors for overlapping shape templates can be produced by learning whitened versions of the generative factors by using singular value decomposition [49]. For example, the letter templates are aligned and then decomposed by singular value decomposition, $\mathbf{P} = \mathbf{U}\Sigma\mathbf{V}$. The whitened templates $\hat{\mathbf{P}} = \mathbf{U}\mathbf{V}$ are encoded into hypervectors similar to (3) and stored in the codebook $\hat{\mathbf{D}} = \Phi \hat{\mathbf{P}}$.

A similar whitening procedure is used to generate the codebook for color, $\hat{\mathbf{C}} \in \mathbb{C}^{N \times 7}$.

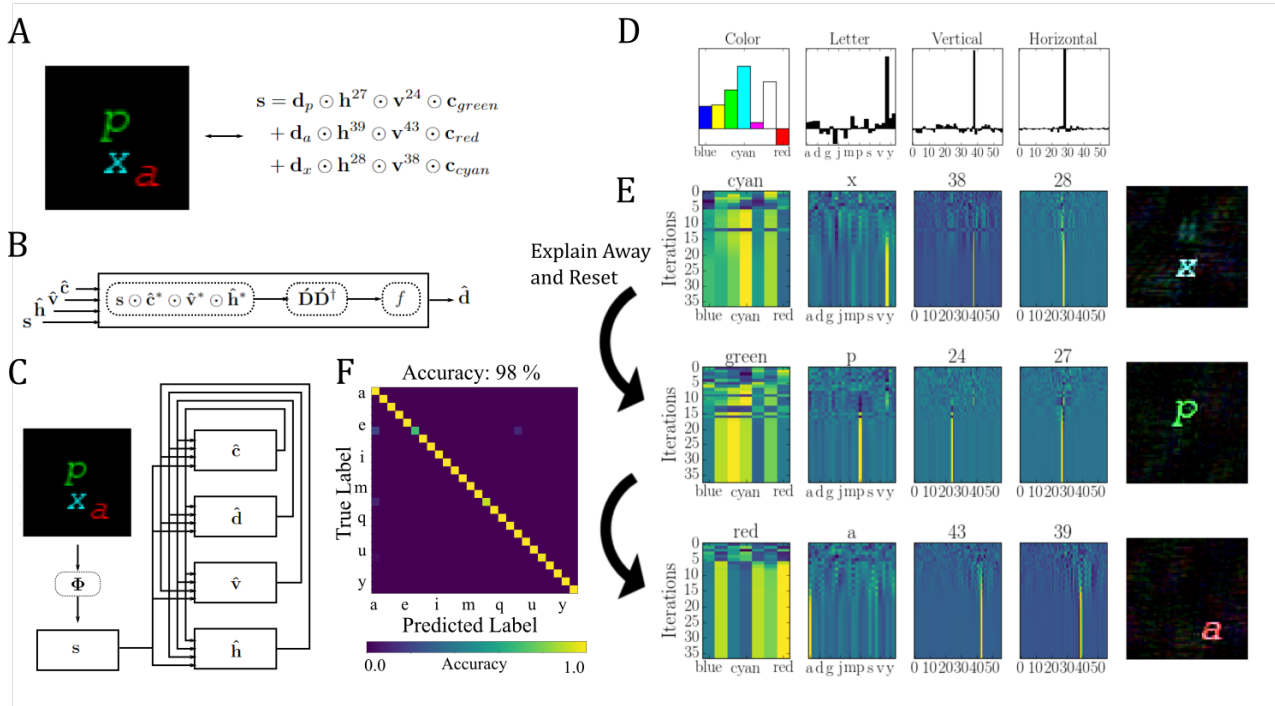


FIG. 1. Resonator network for inferring shape, color, and translation. **A.** A synthetic scene and the VSA representation of the generative model. **B.** A resonator module consists of a binding stage, a clean-up stage, and an activation function. **C.** An input scene created by the generative model is encoded into the VSA space and is the input into the resonator network. The resonator modules communicate their estimates for each factor of variation in the generative model. **D.** The weighted factor estimates in each resonator module can be decoded using the codebooks, and the maximum value is taken as the output. **E.** The four dynamic estimates in the resonator network are each visualized as a heatmap, with time represented vertically and each component represented horizontally. After several iterations, the resonator network converges to a solution and remains stable. Once converged, the component with the largest weight is chosen as the output (top of each panel). The decoded output is visualized to the right of each row. The object is then ‘explained away’ by subtracting the resonator’s estimate from the scene vector. The resonator circuit is reset and converges to another solution, which describes a different object in the scene (rows 2 and 3). **F.** Confusion matrix on translation benchmark task with a single object. Overall performance of the network is 98.4%.

INFERENCE WITH THE RESONATOR NETWORK

A generative model (4) with decorrelated hypervectors enables in principle inference for a given input image. However, inference in generative models is computationally expensive [50] as it involves a combinatorial search across all templates in all possible poses. Conveniently, the VSA formulation (4) permits fast parallel implementations of this search. A given pixel image to be analyzed is first transformed by (1) into a hypervector \mathbf{s} .

Inference of the image content then involves fitting the input vector \mathbf{s} by the best matching templates and transforms contained in the model. Mathematically, this corresponds to constrained optimization, where the constraints are valid code vectors for shape, position and color in (4). In particular, each term of the sum in (4) represents an image component formed by the product of hypervectors that encode object class, color, and pose. Thus, inference essentially is the factorization of \mathbf{s} into specific hypervectors that satisfy the optimization constraints.

This kind of vector factorization problem is very common in VSA algorithms, and recurrent “resonator networks” have been proposed to solve it efficiently [28, 29]. For inference in (4), one constructs the resonator network based on inverting the generative model. The network contains one resonator module that produces an estimate for each factor in the generative model. In each iteration, a module combines all currently available information to update the estimate of its own factor and sends it to the other modules. The available information includes the input vector \mathbf{s} , current guesses of all other factors from the other modules, and the codebook for its own set of factors.

A resonator network module contains three stages: a VSA binding stage, a linear transform, and a component-wise saturation function or normalization (Fig. 1B). The resonator network (5) solves the inference problem dynamically. Starting from random seeds, in each iteration, a module decodes its own factor from \mathbf{s} by unbinding the estimates from all other modules. The decoded vector is then compared to the valid code vectors that are stored in a linear associative

memory. Based on vector similarity, the memory *cleans up* the decoded vector to resemble one or a superposition of valid codebook vectors. After applying the transfer function f , the new estimate is sent to the other modules.

For inference in (4), the dynamic equations of the resonator network are:

$$\begin{aligned}\hat{\mathbf{c}}(t+1) &= f\left(\hat{\mathbf{C}}\hat{\mathbf{C}}^\dagger\left(\mathbf{s}\odot\hat{\mathbf{d}}^*(t)\odot\hat{\mathbf{v}}^*(t)\odot\hat{\mathbf{h}}^*(t)\right)\right), \\ \hat{\mathbf{d}}(t+1) &= f\left(\hat{\mathbf{D}}\hat{\mathbf{D}}^\dagger\left(\mathbf{s}\odot\hat{\mathbf{c}}^*(t)\odot\hat{\mathbf{v}}^*(t)\odot\hat{\mathbf{h}}^*(t)\right)\right), \\ \hat{\mathbf{v}}(t+1) &= f\left(\hat{\mathbf{V}}\hat{\mathbf{V}}^\dagger\left(\mathbf{s}\odot\hat{\mathbf{d}}^*(t)\odot\hat{\mathbf{c}}^*(t)\odot\hat{\mathbf{h}}^*(t)\right)\right), \\ \hat{\mathbf{h}}(t+1) &= f\left(\hat{\mathbf{H}}\hat{\mathbf{H}}^\dagger\left(\mathbf{s}\odot\hat{\mathbf{d}}^*(t)\odot\hat{\mathbf{v}}^*(t)\odot\hat{\mathbf{c}}^*(t)\right)\right),\end{aligned}\tag{5}$$

with $f(\mathbf{x})_i = x_i/|x_i|$ (phasor projection) or $f(\mathbf{x})_i = x_i/\|\mathbf{x}\|_2$ (normalization) (also see Methods) and \mathbf{V} , \mathbf{H} the codebooks of uncorrelated vectors representing vertical and horizontal coordinates of pixels. A linear transform of the form $\mathbf{V}\mathbf{V}^\dagger$ is essentially a linear auto-associative memory [51] that aligns the output to the vectors closest to the input, stored in \mathbf{V} . This distributed dynamic process successively improves the joint estimate of all factors (Fig. 1C). Importantly, individual modules do not settle immediately at a single estimate for their factor (like in a Hopfield memory network). In early iteration steps, they produce a superposition of many possible factors, which enables parallel search through the combinatorics of solutions. In later iterations, the interaction between modules narrows the search down to a single estimate of the identity, pose, and color of one scene component, and the network converges to a stable equilibrium (Fig. 1D, E). For parsing scenes with multiple components, the analysis process is repeated after a previously identified component is subtracted from \mathbf{s} , as part of an outer-loop. This subtraction is similar to “explaining away” or “deflation” [52]. Alternatively, analysis of multiple objects can also be done with several instances of the resonator running in parallel which then compete for the explanation of letters in the image. We call this variant the multi-headed resonator and show results in Fig. 8.

To evaluate performance, we designed several letter recognition benchmark tasks for scene analysis. In Fig. 1F we report results for scenes containing only a single letter, where we measured the accuracy of classifying each letter correctly (see Methods for details). For the recognition task with all 26 letters, the network was 98% accurate at identifying letter templates regardless of color or translation with the network $N = 10,000$.

The complexity of the scene analysis problem can be quantified by the total combinations that the system must search over. In the benchmark, there are 26 letters and 7 colors and an image resolution of 64x64 pixels, giving a combination space of 745,472. This amount is much less than the operational capacity (which for $N = 12,000$ is about 100 million) [28] where the resonator network is expected to have nearly 100% accuracy. Importantly, note that the operational capacity in a resonator was measured for uncorrelated vectors, and performance on scene analysis will be different due to correlations between the generative objects. The whitening removes correlations when letters are in their default position, but not when they are in arbitrary relative positions.

INFERRING ROTATION AND SCALE TRANSFORMS

The approach can easily be applied to scenes where a centered object is transformed by rotation and scaling. We will use the fact that rotation and scaling in Cartesian space becomes translation in log-polar space (Fig. 2 A), with $\mathbf{L} \in \mathbb{R}^{L_m L_r \times P_x P_y}$ the log-polar transform matrix. Thus in log-polar coordinates, the binding operation becomes the equivariant transform for rotation and scaling. From a generative model of rotated and scaled object templates in log-polar coordinates, we can construct the following resonator network (Fig. 2 B):

$$\begin{aligned}\hat{\mathbf{d}}(t+1) &= f\left(\hat{\mathbf{D}}_{\mathbf{L}}\hat{\mathbf{D}}_{\mathbf{L}}^\dagger\left(\mathbf{s}_{\mathbf{L}}\odot\hat{\mathbf{r}}^*(t)\odot\hat{\mathbf{m}}^*(t)\right)\right), \\ \hat{\mathbf{r}}(t+1) &= f\left(\mathbf{R}\mathbf{R}^\dagger\left(\mathbf{s}_{\mathbf{L}}\odot\hat{\mathbf{d}}^*(t)\odot\hat{\mathbf{m}}^*(t)\right)\right), \\ \hat{\mathbf{m}}(t+1) &= f\left(\mathbf{M}\mathbf{M}^\dagger\left(\mathbf{s}_{\mathbf{L}}\odot\hat{\mathbf{d}}^*(t)\odot\hat{\mathbf{r}}^*(t)\right)\right).\end{aligned}\tag{6}$$

Here, the codebooks \mathbf{R} and \mathbf{M} contain the vector symbols for each log-polar coordinate, e.g. $\mathbf{R} = [\mathbf{r}^1, \mathbf{r}^2, \dots, \mathbf{r}^{L_r}]$, $\mathbf{M} = [\mathbf{m}^1, \mathbf{m}^2, \dots, \mathbf{m}^{L_m}]$. The codebook $\hat{\mathbf{D}}_{\mathbf{L}} \in \mathbb{C}^{N \times L_m L_r}$ contains the bindings of these index hypervectors for log-polar coordinates akin to $\hat{\mathbf{D}}$ (3). Further, the index vector \mathbf{r} is designed with a toroidal similarity structure, such that translated pixels wrap around the image. This is achieved by constraining the phases of \mathbf{r} to the N^{th} roots of unity like in a Fourier transform [27]. Similarly, the codebook $\hat{\mathbf{D}}_{\mathbf{L}} = \hat{\mathbf{D}}_{\mathbf{L}}\mathbf{L}\hat{\mathbf{D}}$ contains the whitened letter patterns in the log-polar space.

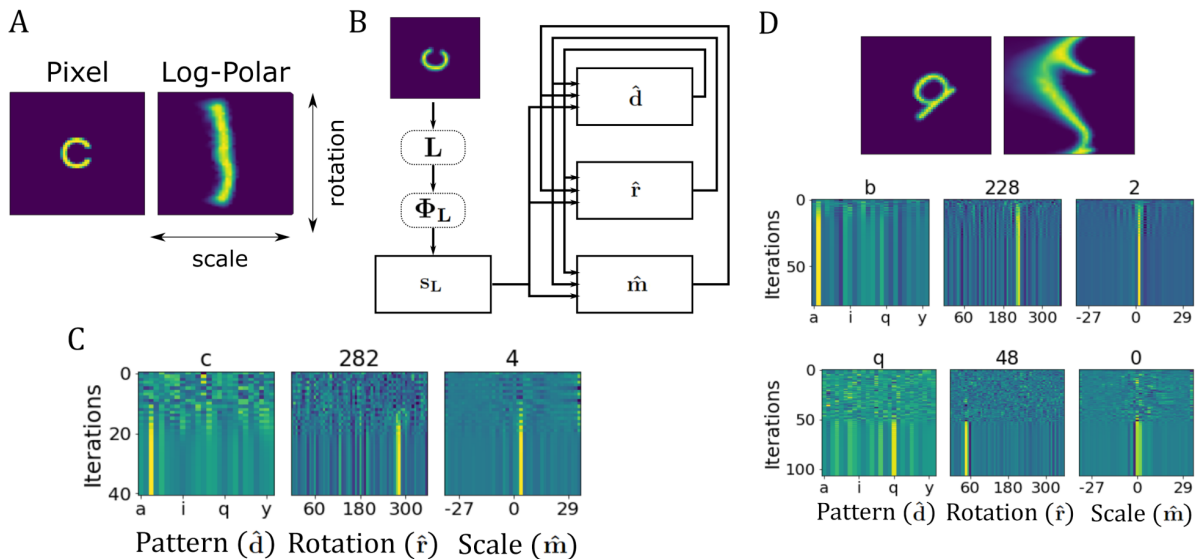


FIG. 2. Resonator network for rotation and scale. **A**. Translation in log-polar space results in rotation and scaling in Cartesian space. **B**. Diagram of resonator network for inferring shape, rotation, and scaling of input images. **C**. Example of network dynamics. **D**. Symmetries of the template lead to ambiguous factorizations. Two examples of the resonator network are shown with different random initializations. The resonator network will converge to one of the ambiguous factorizations (letters ‘b’ or ‘q’).

Figure 2 displays an example of inference with the resonator network (6) of an image. The simulation results highlight a general problem of using generative models for analyzing a scene. Often, image components can have more than one valid explanation because of inherent symmetries. In this case, different letter templates can become identical when rotated by different angles, such as ‘b’ and ‘q’. Thus, the analysis of scenes with these letters becomes ambiguous. For ambiguous inputs, the resonator network selects one solution but will not indicate the existence of alternative solutions. Which of the solutions is selected depends on random initialization and other noise sources (Fig. 2D).

ANALYZING SCENES COMPOSED FROM RIGID, NON-COMMUTATIVE TRANSFORMS

The next step toward analyzing realistic scenes is the ability to identify object templates transformed by arbitrary rigid transforms, including translation, rotation, scale, and color. We will describe a resonator network with a novel architecture for solving this type of image analysis.

The generative model of an image synthesized from rigid transforms of shape templates can be written as:

$$\mathbf{s} = \sum_i \mathbf{c}_{c_i} \odot \mathbf{h}^{x_i} \odot \mathbf{v}^{y_i} \odot \mathbf{\Lambda}^{-1}(\mathbf{r}^{r_i} \odot \mathbf{m}^{m_i} \odot \mathbf{d}_{p_i}), \quad (7)$$

where $\mathbf{\Lambda} = \mathbf{\Phi}_L \mathbf{L} \mathbf{\Phi}^\dagger$ is the log-polar transform matrix in the high-dimensional VSA space. For performing inference in this generative model, one can again construct a corresponding resonator network. Describing the six factors in (7), the network consists of six fully connected factor modules that all require coordinate transforms, $\mathbf{\Lambda}$ or $\mathbf{\Lambda}^{-1}$, in their binding stages, see Methods (10). Interestingly, the structure of these equations suggests a partitioned network architecture that avoids redundant coordinate transforms. The final network consists of two partitions, each fully connected internally: one operating in Cartesian and one in log-polar coordinates. Each partition has an additional module that serves as the communication bridge between the partitions. Conveniently, the bridge modules have exactly the same internal stages as other resonator modules, a binding stage followed by a linear transform (f is the identity function in this case):

$$\hat{\mathbf{l}}(t+1) = \mathbf{\Lambda}^{-1}(\hat{\mathbf{r}}(t) \odot \hat{\mathbf{m}}(t) \odot \hat{\mathbf{d}}(t)), \quad (8)$$

$$\hat{\mathbf{p}}(t+1) = \mathbf{\Lambda}(\mathbf{s} \odot \hat{\mathbf{c}}^*(t) \odot \hat{\mathbf{h}}^*(t) \odot \hat{\mathbf{v}}^*(t)). \quad (9)$$

En lieu of writing the entire equation system, we describe the schematic of the partitioned resonator network in Fig. 3A and its relations to the resonator networks (6) and (5). The *log-polar partition*, the right column of modules in Fig. 3A,

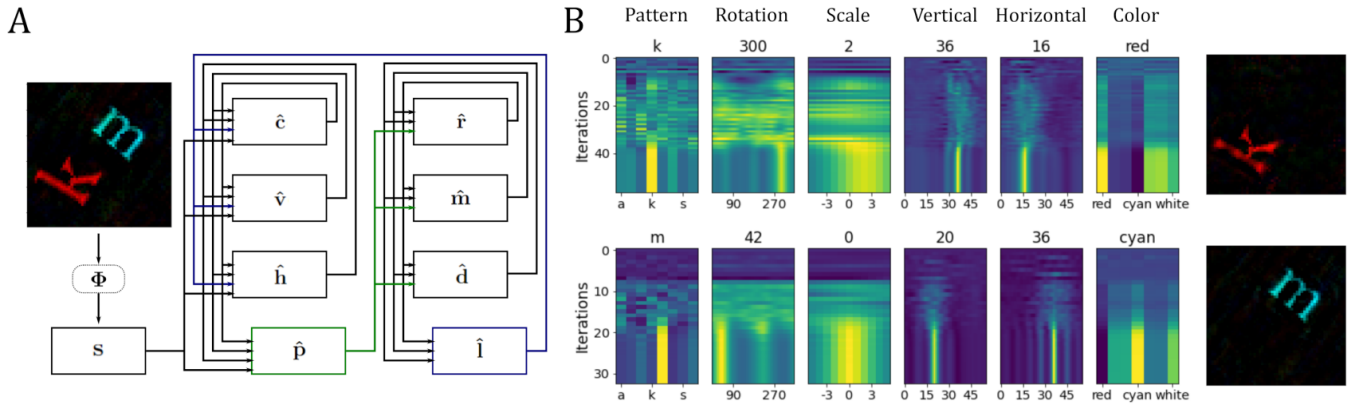


FIG. 3. The hierarchical resonator network for inferring rigid transforms. **A.** Schematic diagram of the hierarchical resonator network. **B.** The dynamics of the resonator network identifying objects in the input scene.

contains the “top-down” bridge module (8) and the modules from (6). The top-down bridge module (8) produces $\hat{\mathbf{I}}$, the estimate of a rotated and scaled shape computed by the log-polar partition, transformed to Cartesian coordinates. The *Cartesian partition*, the left column of modules in Fig. 3A, contains the modules from (5), but the module with output $\hat{\mathbf{d}}$ replaced by the “bottom-up” bridge module (9). The previous input from $\hat{\mathbf{d}}$, which is an estimate of the letter shape, is replaced by the top-down signal $\hat{\mathbf{I}}$, which is an estimate of the letter shape with a particular rotation and rescaling. The bottom-up bridge unit (9) produces $\hat{\mathbf{p}}$, which removes the estimated translation and coloring from the input and transforms a centered version of the input into log-polar coordinates. This in effect replaces the input for (6).

We call the architecture in Fig. 3A the *hierarchical resonator network* because the bidirectionally connected partitions assume different hierarchy levels by the definition of Felleman and Van Essen [53]. The Cartesian partition receives direct input according to a lower level, while the log-polar partition is one removed from the sensory input according to a higher level. The log-polar partition also holds the discrete shape templates in memory, the arguably most abstract aspect of the image components.

A successful example of inference with the hierarchical resonator network is shown in Fig. 3B. The upper row shows a factorization process, revealing the letter “k”, and the lower row shows a second factorization process, revealing the letter “m”. Note how the estimates of all factors are undecided and blurry in early iteration steps and become sharp quite suddenly during iteration.

An unsuccessful example of inference is shown in Fig. 4. In this case, the first factorization falsely explains the arched portion of the “m” with a rotated “s”. After subtraction of the “s” there are still parts of the “m” left, which the second factorization run falsely explains as an “a”. This failure in analyzing one image component would probably not prevent a third factorization run from correctly identifying the second image component as a “k” (experiment not shown).

We performed a similar set of benchmark experiments for the scene understanding task with six degrees of freedom. We constrained the task to a subset of 10 letters and about half ($\pm 89^\circ$) of the rotations, in order to reduce the complexity and the number of ambiguous factorizations, as many of the ambiguities are due to 180° rotational symmetry. Note that with 6 factors of variation, the combinatorial space has expanded to over 100 million combinations that the network must search through, meaning the problem is much more challenging. In our benchmark experiment, the system identifies the correct letter with an accuracy of 84% (Fig. 4D).

When the network fails, it often converges to a spurious solution which is composed of a complex mixture of generative factors. Even though these examples did not recover the true generative factor, the spurious solutions still have significant correlations with the input (Fig. 4E). In the Methods, we describe some modifications to the resonator network dynamics that mitigate these errors, such as adding non-linearities that encourage sparse solutions. However, these modifications cannot completely eliminate this issue which has also been reported in other generative model approaches for scene analysis, e.g., [33].

IMPLEMENTATION WITH SPIKE-TIMING-BASED PHASOR NEURONS

Finally, we implement the core elements of our model for visual scene analysis as an SNN with an efficient spike-timing code running on Intel’s Loihi neuromorphic research chip [41]. As a proof of concept, we only include the factors for

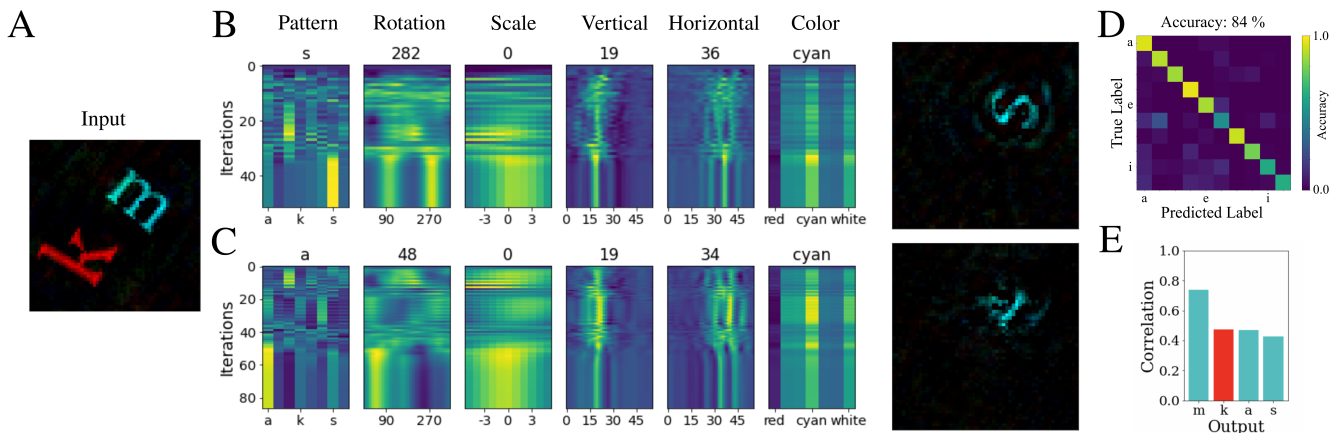


FIG. 4. Local minima in the hierarchical resonator network. **A**. Input image. **B**, **C**. Two incorrect runs of the network are visualized. Often the network converges to solutions where a shape is incorrectly fit into the explanation of the scene. Note how there are multiple peaks in some of the factors, which induces complicated overlaps of stored patterns. **D**. Confusion matrix of object classes.

E. Correlations between the incorrect explanations and the input are on par with the correct explanations (right panel).

translation ($\hat{\mathbf{h}}, \hat{\mathbf{v}}$) and the pattern ($\hat{\mathbf{d}}$) of the equation system (10), see Fig. 5A. The components of the complex VFA vectors are represented by the spike timing of integrate and fire neurons [54]. Specifically, the spike time within a predefined cycle window of length T represents the phase of a complex number (see Fig. 5B). Conveniently in (10), magnitudes of complex numbers do not have to be represented, as the non-linear function f is the phasor-projection, and the binding operation does not change phasor magnitudes.

The SNN resonator network on Loihi consists of 3-factor modules that are connected recurrently, as shown in Fig. 5. The input spike generator converts the input vector \mathbf{s} into spikes and transmits these spikes into the binding stages of the modules (Fig. 5B). Each binding stage performs a neuron-wise complex phase shift based on its inputs (Fig. 5C), implementing the FHRR binding operation. The cleanup module (Fig. 5D) performs a matrix multiplication with the auto-associative matrix, e.g., $\mathbf{H}\mathbf{H}^\dagger$. An additional gate stage in each module controls the flow of spikes through the network, making sure that the network maintains the correct timing. To implement phase addition in FHRR binding, the spike delay of a neuron has to represent the sum of spike delays of two inputs. Input-dependent firing delays can be achieved on Loihi through a multi-compartment integrate-and-fire model (Fig. 5B). Two of the compartments, “aux” and “soma”, act like clocks with a cycle time of T by simply integrating constant inputs and resetting when they reach a threshold. The first input (s) to the soma compartment resets the soma’s clock. The second input acts as a gate from the aux neuron to the dendrite. When the gate is opened by the second input spike, the aux state is added to the soma state, delaying the soma from reaching the spike threshold and thus shifting the timing of the output spike (as illustrated in Fig. 5C). Note that this implementation of phase addition is specific to the Loihi hardware.

The complex-valued matrix-vector product is implemented through synaptic connections with time delays representing the phase of the synaptic weights (Fig. 5D). The summation of complex numbers corresponds to the integration of sine waves [54]. On Loihi, we combine inhibitory currents with a delayed excitatory current evoked by each input spike to create an approximate sine wave in the membrane potential. This mechanism is illustrated for just 2 inputs in Fig. 5E, but the approximation becomes more robust with more input neurons.

After the cleanup, the spikes representing each factor are fed back to the binding stage. The input to the binding stage has to be timed correctly because the shift module needs multiple cycles for its computation. To provide proper timing, the gate stage between modules blocks all spikes until it is opened by a regularly occurring control input. The gating between pairs of neurons is implemented by a group of neurons with an inhibitory bias current that prevents spiking, which is counteracted by disinhibition when the gate is opened for one cycle. One iteration in the resonator network takes in total 5 cycles on Loihi. In our experiment (Fig. 5), we set the cycle time $T = 16$ timesteps, i.e. the phasors have 16 discrete phases.

Fig. 6 shows a comparison between Loihi and a CPU in terms of energy and latency. While Loihi is slower, it is orders of magnitude more energy efficient (Fig. 6A and B). For the largest network size, Loihi is 171 times more efficient in terms of energy-delay-product (Fig. 6C) and scales better than the CPU for increasing network size, likely due to sparse, event-based matrix multiplication. The comparison uses cleanup with a full $N \times N$ auto-associative matrix on both Loihi and the CPU. For small numbers of symbols, it is computationally advantageous to first multiply with the decoding matrix (e.g., H^\dagger) and then with the encoding matrix (H). The intermediate result can, however, not

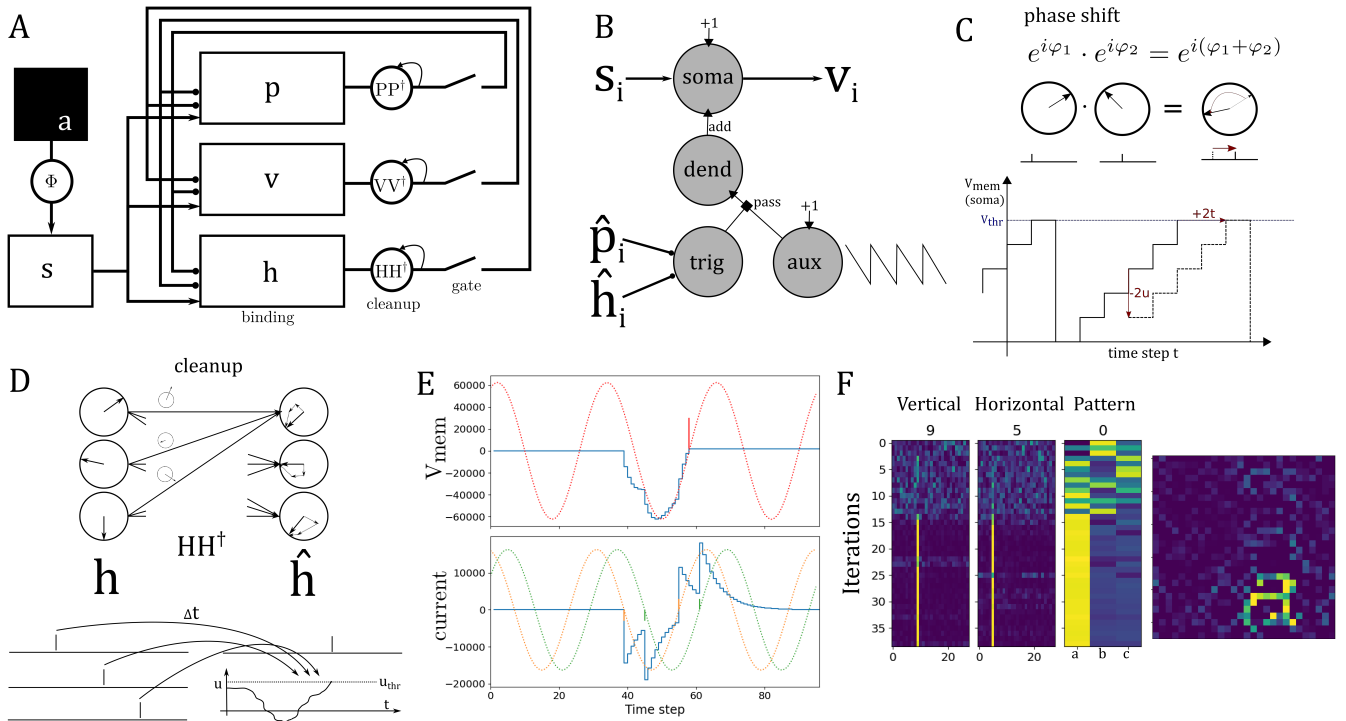


FIG. 5. The resonator network on the Loihi neuromorphic hardware with phasor integrate and fire neurons. **A.** Schematic of the resonator architecture implemented on Loihi. **B.** Implementation of the (un-)binding module (complex phase-shifting) as a 4-compartment neuron on Loihi. This is repeated for each element of the vector. Input from $\hat{\mathbf{p}}$ and $\hat{\mathbf{h}}$ triggers a “pass” operation that lets current from an auxiliary oscillating compartment flow into the dendritic compartment. The soma integrates a constant current so that the neuron fires regularly, but it can be delayed by the inhibitory input from the dendritic compartment. **C.** Mechanism of the phase shift. Here, the soma membrane potential is inhibited by 2, so it will reach the threshold two timesteps later, corresponding to a phase shift of 2. The inset at the top shows the equation of complex multiplication, its phasor representation, and the corresponding spike timing in phasor I&F neurons. **D.** Mechanism of the cleanup module. Top: Phasor representation of the complex matrix multiplication of \mathbf{h} with the cleanup matrix \mathbf{HH}^\dagger . Each complex matrix element corresponds to a synapse with a weight and a phase. In the receiving neuron, the weighted phases are summed up. Bottom: The same mechanism with I&F phasor neurons. Complex phases correspond to spike timing and complex synapses to synapses with a weight and a delay. This works as the complex addition can be represented as the addition of sine waves (see panel E.) **E.** Mechanism of the complex adder with I&F phasor neurons. The neuron receives two inputs at different phases (orange and green). Each input elicits an inhibitory postsynaptic current with a delay of $1/2 T$ and an excitatory postsynaptic current with a delay of T . The current gets integrated into the membrane potential, which approximates a sine wave. Here, the red output wave is the sum of the orange and the green input waves. In blue, the membrane potential and input current of the Loihi neuron are shown. Note how the membrane potential follows the red output sine wave and the neuron spikes at the 0-crossing (the red spike signals the phase). The spiking threshold is set to 0. Small and large amplitude oscillations will produce spikes, which computes the phasor-projection non-linearity f (5)

. **F.** States of the resonator on Loihi over 40 iterations and reconstructed image from resonator states.

be represented in a phasor encoding without amplitudes. We are working on an encoding that is able to represent amplitudes on Loihi 2, the next generation of the Loihi chip, which will improve the scalability of the architecture.

DISCUSSION

We have described a novel algorithm for inference in generative models and its neuromorphic implementation with an efficient spike-timing code [54] on modern spiking neuromorphic hardware [41]. This algorithm is validated on the problem of analyzing synthetic visual scenes, and we extend the work in our companion paper to demonstrate an application to a real-world task, visual odometry in robotics [55].

Inference in generative models – also known as “analysis by synthesis” – is a powerful method for invariant pattern analysis, but it is infamously computationally expensive [50]. Our proposal to make it tractable hinges on vector

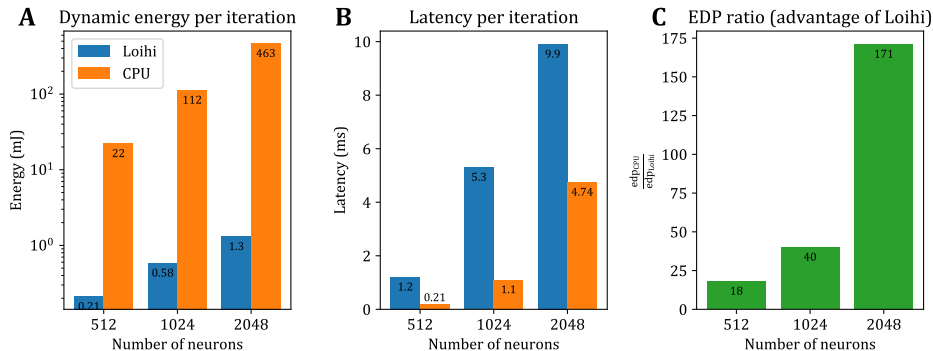


FIG. 6. **A.** Logarithmic plot of the dynamic energy per iteration of the resonator with three factors on Loihi and a CPU for different network sizes (number of elements of the VSA vectors). **B.** Time used for one iteration of the resonator on Loihi and a CPU **C.** Energy-delay-product (EDP) of the CPU divided by the EDP of Loihi. Loihi is 41 to 266 times more efficient depending on the size of the resonator and gains an advantage for larger network sizes.

binding, an operation offered by VSAs but not by conventional neural networks, and a recent proposal of resonator networks, modular recurrent networks for efficient vector factorization [28, 29]. Three key ideas enable invariant pattern recognition with resonator networks on neuromorphic hardware. The first idea is to develop data encoding schemes and generative models that make binding the equivariant operator for a factor of variation, such as image translation. The second idea addresses the existence of multiple factors of variation that are non-commutative, like translation versus image rotation and scaling. Inspired by a classical method for image registration, the Fourier-Mellin transform [56–58], we propose a novel hierarchical resonator network. The network consists of two partitions of fully connected modules, one operating in Cartesian, the other in log-polar coordinates, coupled by a pair of bridge modules. Binding is the equivariant operation for translation in one partition for rotation and scaling in the other. The third idea is to use multi-compartment neuron models for implementing the complex vector binding operation in a spike-timing code on neuromorphic hardware.

Achieving translation-invariant object classification has been a long-standing problem for machine learning and neural networks [59, 60]. Deep learning essentially uses a combination of convolution and pooling operations [61], which introduces some forms of translation invariance, but surprisingly does not achieve fully translation-invariant pattern recognition [62]. Our own prior work on scene understanding explored deep learning for mapping images to VFA representations of the scene content [28, 63]. While technically successful, our results echoed problems reported by others, such as short-cut learning [64]. General invariance to transformations like translation are not naturally learned by supervised training, and many network architectures fail with input transformations not covered by the training data [65]. Efforts to impose an inductive bias into the network to encourage translation invariance have shown promise, such as data augmentation [66], but they still fall short of general translation invariance. Our approach inverts a generative model for objects, which, compared to deep neural networks, is transparent and also does not require any training. Further, our solution can be applied to a variety of visual tasks as it extracts both, the invariant and equivariant representation from the stimulus.

The concept of scene analysis by inference in generative models is well established and would enable invariant object recognition naturally [9]. However, proposals for concrete neural models that probe and explore this concept are quite recent. One example is the map-seeking circuit (MSC) [33], a feedback multi-layer network that has been demonstrated on scene analysis and also has been successful in adaptive optics applications [67]. Our method shares with the MSC the use of superposition and content-addressable memory for estimating transforms. The main difference lies in the implementation of image transforms and how inference is computed. Further, bilinear models [35, 36, 39] have been proposed to extract two factors of variation from an input. Bilinear models differ from our model in that they use standard optimization methods for the computationally expensive inference procedure. The work on bilinear models mainly focused on how to learn the components in a generative model from input – whereas here we investigated inference with a known generative model. During the learning procedure, bilinear models use singular value decomposition (SVD) of the input samples to construct the generative model. The use of SVD for decorrelating representations we have adopted from this literature. Further by formulating the generative model of objects in the VSA framework, our approach can use resonator networks to perform inference with more than two factors of variation efficiently.

When evaluated on the analysis of simple synthetic scenes, our model succeeds most of the time but can also fail for several reasons, most of them common to other generative model approaches.

For the full benchmark problem with 6 factors of variation, the performance of the network is 84%, lower than 98% achieved for the 4-factor benchmark problem. The combinatorics of the 6-factor problem is much higher than the 4-factor problem, however, the operational capacity of the resonator network [29], discussed below, is not the limiting factor. The primary reason for the mistakes of the network is spurious matches involving complex mixtures of generative factors. Like the ambiguity between a ‘p’ versus a rotated ‘d’, the spurious matches reconstruct the input with high quality, correctly capturing location and color, but using shape primitives of the wrong class.

One cause of spurious matches is that the generative model should choose only one object, and this is currently not reflected by an appropriate prior in our model. We explore the addition of sparsity mechanisms to the resonator dynamics that encourage simple scene explanations (see Methods), however, an exact incorporation of priors would likely improve the performance even further. Another cause for spurious matches that is harder to fix is mutual correlations between shape templates. While we do eliminate correlations between shape templates in their default pose, strong correlations between templates can still arise if their relative poses differ.

Pairwise alignment of the letters for the whitening makes sure that the correlations for the most relevant shift are removed, but there are still many possible spurious explanations that act as local minima for the resonator. Therefore, we tested alignment and annealing procedures and observed improved performance (shown in table I).

The earlier analysis of resonator networks [29] assumed the total absence of correlations between code vectors and therefore provides an upper bound of the complexity in a scene that a resonator of a given size can handle. According to the theory, the number of combinations that can be searched scales with the square of network size, i.e., $M_{max} \propto N^2$. This scaling behavior holds for different numbers of factors (the proportionality constant slightly drops for an increasing number of factors). For scene analysis, the combination that needs to be searched over is the product of all the variations: number of objects, number of possible positions, and number of colors. For scenes with small objects that extend just a few pixels, the theory in [29] predicts that the dimension of the hypervectors has to grow roughly with the square root of the number of pixels – given the number of possibilities in all other factors of variation stays constant. The number of hypervectors needed is only $P_x + P_y$ since the network architecture divides each pixel dimension into separate modules.

The presented results demonstrate that the combination of neuromorphic hardware and recent developments in VSA offers a tractable approach to scene analysis through a generative model. We believe the approach with hierarchical resonator networks can extend beyond synthetic scenes used in our benchmark. For instance, one direction we are currently investigating is to describe a larger variety of visual objects in the generative model by using sparse features rather than full-letter templates. The path towards neuromorphic analysis of naturalistic scenes, useful for embodied agents, will require further revising the generative model (7), such as adding priors, 3D shape models with 3D transforms [68] and effects of occlusion [69]. The advantage of VSA over traditional artificial neural networks (ANN) as a programming framework for emerging hardware, such as neuromorphic hardware, has been emphasized before [70]. Our VSA model with dense complex vectors already demonstrates this advantage – the resulting spike-timing code requires much lower spike traffic than a rate code resulting from ANN models. There are also other interesting options. For example, an implementation of the proposed VSA model with spatially sparse complex vectors [40] would have even lower spike traffic, as well as reduced memory requirements for storing the codebooks. However, this option would incur somewhat higher computational costs, because the binding operation between sparse vectors is computationally more expensive [71].

Although addressing technical applications, our work also has implications for neuroscience. The feature binding problem of neuroscience is solved by the binding operation in VSA-type models, but the original VSA models did not offer a solution to how the binding operation could be implemented by neurons of the brain. Our work suggests an efficient implementation of binding and visual perception with spiking neurons. In particular, the phasor neuron proposed for implementing binding corresponds to a velocity-controlled oscillator (VCO), which has been proposed as a model for place and grid cells [72, 73]. Without input, the neuron fires periodically, and the spike phase is constant. Input slows down the oscillation by inhibition leading to a phase shift. Thus, our model makes specific predictions about computational roles of spike timing and oscillations that can be tested in neuroscience data and experiments.

METHODS

Details of simulation experiments

Simulation experiments using the resonator network were implemented in Python using Numpy and PyTorch. The vector dimensions used for the benchmarking experiments are $N = 10,000$ for the translation task, and $N = 16,384$ for the Cartesian module and $N = 22,680$ for the log-polar module of the hierarchical resonator in the rigid transform task.

The resonator network is initialized to either a random state or each factor is initialized to the mean of all its codebook vectors (leading to slightly more reliable performance).

The full dynamic equations for the hierarchical resonator network:

$$\begin{aligned}
\hat{\mathbf{c}}(t+1) &= f\left(\hat{\mathbf{C}}\hat{\mathbf{C}}^\dagger\left(\mathbf{s} \odot \hat{\mathbf{h}}^*(t) \odot \hat{\mathbf{v}}^*(t) \odot [\mathbf{\Lambda}^{-1}(\hat{\mathbf{r}}(t) \odot \hat{\mathbf{m}}(t) \odot \hat{\mathbf{d}}(t))]^*\right)\right), \\
\hat{\mathbf{h}}(t+1) &= f\left(\hat{\mathbf{H}}\hat{\mathbf{H}}^\dagger\left(\mathbf{s} \odot \hat{\mathbf{c}}^*(t) \odot \hat{\mathbf{v}}^*(t) \odot [\mathbf{\Lambda}^{-1}(\hat{\mathbf{r}}(t) \odot \hat{\mathbf{m}}(t) \odot \hat{\mathbf{d}}(t))]^*\right)\right), \\
\hat{\mathbf{v}}(t+1) &= f\left(\hat{\mathbf{V}}\hat{\mathbf{V}}^\dagger\left(\mathbf{s} \odot \hat{\mathbf{c}}^*(t) \odot \hat{\mathbf{h}}^*(t) \odot [\mathbf{\Lambda}^{-1}(\hat{\mathbf{r}}(t) \odot \hat{\mathbf{m}}(t) \odot \hat{\mathbf{d}}(t))]^*\right)\right), \\
\hat{\mathbf{d}}(t+1) &= f\left(\hat{\mathbf{D}}_L\hat{\mathbf{D}}_L^\dagger\left([\mathbf{\Lambda}(\mathbf{s} \odot \hat{\mathbf{c}}^*(t) \odot \hat{\mathbf{h}}^*(t) \odot \hat{\mathbf{v}}^*(t))] \odot \hat{\mathbf{r}}^*(t) \odot \hat{\mathbf{m}}^*(t)\right)\right), \\
\hat{\mathbf{r}}(t+1) &= f\left(\hat{\mathbf{R}}\hat{\mathbf{R}}^\dagger\left([\mathbf{\Lambda}(\mathbf{s} \odot \hat{\mathbf{c}}^*(t) \odot \hat{\mathbf{h}}^*(t) \odot \hat{\mathbf{v}}^*(t))] \odot \hat{\mathbf{d}}^*(t) \odot \hat{\mathbf{m}}^*(t)\right)\right), \\
\hat{\mathbf{m}}(t+1) &= f\left(\hat{\mathbf{M}}\hat{\mathbf{M}}^\dagger\left([\mathbf{\Lambda}(\mathbf{s} \odot \hat{\mathbf{c}}^*(t) \odot \hat{\mathbf{h}}^*(t) \odot \hat{\mathbf{v}}^*(t))] \odot \hat{\mathbf{d}}^*(t) \odot \hat{\mathbf{r}}^*(t)\right)\right).
\end{aligned} \tag{10}$$

The codebooks $\hat{\mathbf{D}}_L \in \mathbb{C}^{N \times 26}$ and $\hat{\mathbf{C}} \in \mathbb{C}^{N \times 7}$ are formed from whitened templates projected into the high-dimensional vector space. Specifically, the templates are transformed into log-polar coordinates and decomposed by the singular value decomposition, i.e., $\mathbf{P}_L = \mathbf{L}\mathbf{P} = \mathbf{U}_L\mathbf{\Sigma}_L\mathbf{V}_L$. The whitened templates are given by $\hat{\mathbf{P}}_L = \mathbf{U}_L\mathbf{V}_L$, which is then projected into the high-dimensional space by $\hat{\mathbf{D}}_L = \mathbf{\Phi}_L\hat{\mathbf{P}}$. A similar whitening procedure is applied for the colors to produce $\hat{\mathbf{C}}$, but not for the other codebooks.

In the resonator for the translation task, the letter template images are aligned for the whitening procedure to make sure the whitening removes the correlation at the most relevant shift of the letters. For instance, for the whitening of each letter image, all other letters are aligned (pairwise to the respective letter) by finding the best overlap using image registration by phase correlation in the 2d Fourier domain [56–58]. Then, whitening is performed over the letter image and all pairwise aligned other images. The respective whitened image is added to the codebook and all other images are discarded. This is repeated for all letter images. For the HRN, this alignment-whitening procedure is omitted as it is impossible to capture all relevant correlations and therefore performance would not improve. For the HRN, letters are just aligned before adding them to the codebook.

In the HRN, rotation as an operation must have the correct topology for its representation – i.e., rotation by 360° results in the same image. This is done by ensuring that the representation vector \mathbf{r} also has circular topology. The circular topology is encoded by defining a periodic kernel for the representation \mathbf{r} , where the random phases of the components of \mathbf{r} are sampled from a discrete probability distribution [27]. Specifically, the phase circle is divided into L_r discrete samples and each component of \mathbf{r} is one of these samples, $r_i \in \{e^{i2\pi k/L_r} \forall k \in \{1, \dots, L_r\}\}$.

Beyond the dynamics described in equation (10), we include some modifications to improve performance. One modification is hysteresis in the update dynamics, where some fraction of the past state is included in the next update, i.e.:

$$\mathbf{d}(t+1) = (1 - \gamma)\mathbf{d}(t) + \gamma f(\hat{\mathbf{D}}\hat{\mathbf{D}}^\dagger(\mathbf{s} \odot \hat{\mathbf{h}}^*(t) \odot \hat{\mathbf{v}}^*(t))) \tag{11}$$

with γ controlling the rate of the hysteresis.

Another modification is adding a non-linearity, such as a ReLU, polynomial exponent, or softmax function, to encourage sparsity. As well, we incorporated external noise (η) to reduce the stability of spurious local minima:

$$\mathbf{d}(t+1) = f(\hat{\mathbf{D}}p(\hat{\mathbf{D}}^\dagger(\mathbf{s} \odot \hat{\mathbf{h}}^*(t) \odot \hat{\mathbf{v}}^*(t))) + \eta, \tag{12}$$

Our experiments show that a combination of a ReLU and polynomial exponent $p(\mathbf{x}) = \mathbf{ReLU}(\mathbf{x})^k$, performs best. The ReLU serves two purposes: It avoids negative factor pairs and it acts as a threshold to improve the cleanup. Note that without ReLU, the resonator network can converge to a solution where an even number of factors are negative, a problem that can be fixed by taking absolute values as the final outputs. The k parameter controls the amount of superposition of different possible solutions, i.e. the sparsity. It can be set to values below 1 to weaken the cleanup or to values well above 1 to achieve a stricter cleanup (like an argmax or winner-take-all for high k s). In the case of the translation resonator, $k = 1$ proved to be sufficient, while in the hierarchical resonator, at least one factor, (we chose the angle factor), needs a larger k , typically above 3. Furthermore, after each iteration, the resonator states (with the exception of the pattern state (\mathbf{d})) are phasor projected (f), i.e., magnitudes of all vector components are set to 1. Additionally, complex Gaussian distributed noise is added to the state ($\eta \in \mathbb{C}^N \sim \mathcal{N}(0, \sigma)$) with $\sigma = 1$ in the resonator for the translation task and $\sigma = 0$ in the hierarchical resonator’s log-polar module. In the last 2 iterations of each pass, however, the noise is turned off to get a cleaner readout.

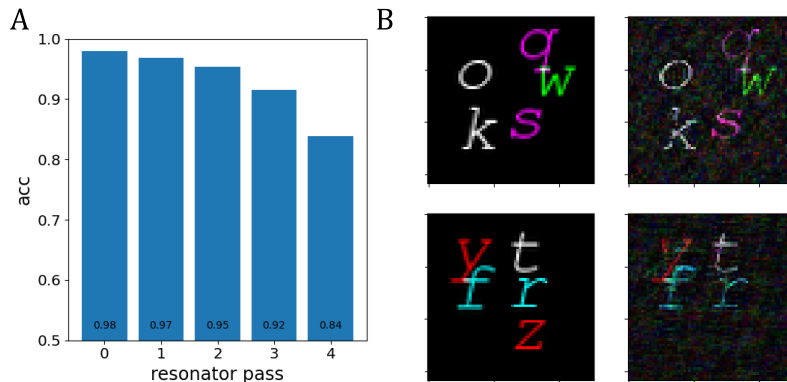


FIG. 7. Benchmarking of the resonator network for the letter translation task with 5 random letters, and 1000 random samples. **A.** Letter classification accuracy for each of the 5 passes. **G-H.** Two random example input images (left) and the reconstruction from the final resonator states (right), by adding all final states together. All letters were reconstructed correctly, apart from the red 'z' in the second image.

Details of performance benchmarking

To benchmark the model, images with a given number of letters are created. Letters, locations, and rotations are chosen randomly. For the translation task, letters are chosen randomly from all 26 letters of the English alphabet; for the rotation task, from the first 10 letters of the alphabet. We use the font 'TlwgTypewriter-Oblique' at a font size of 26 in an image of 64x64 pixels. The letters are shifted using `scipy.ndimage.shift` by a random floating point number uniformly distributed between -19 and +19, i.e. with a margin of 13 pixels from the border to avoid cropping of letters. To avoid overlaps between letters, after adding a letter to an image, the new image is compared with the old image. If at least one pixel overlaps, the random choice of vertical and horizontal translation of the newly added letter is repeated. If no non-overlapping image has been found after 20 repetitions of this process, the image is used as it is in the 20th repetition (with the overlap). Note that letters can still look like they overlap if they have colors that are non-overlapping such as red and green.

To benchmark the different model variants, we report an accuracy measure based on the percentage of correct classifications of the letter identity. We chose this measure as it is straightforward to calculate and compare and because getting the letter identity correct usually also means that the other factors are estimated well (the opposite is not true). The letter output of the resonator is the argmax of the state readout (product of the letter factor codebook and the factor state).

For the tasks with several letters in the input image, a classification is counted as correct if the letter output corresponds to any of the letters in the image. One instance of the correctly guessed letter is then removed from the list so that the next pass has to guess one of the remaining letters correctly in order to count as a correct classification.

To find the best parameters for the different model variants, we perform a hyperparameter search. Starting from a manually tuned network, we perform a sweep for each parameter separately. Parameters that are optimized in this manner are the noise variance (σ), the state update ratios for each set of states separately (γ), and the polynomial exponents (k). The hyperparameter search is performed with a different random seed, i.e. a different dataset and a different random codebook than the test seed that is only used to test the network on a given number of samples.

Additional experiments

Analysis of multiple objects. Fig. 7 shows results for the resonator solving the letter translation task with five letters. The performance in the first pass is almost the same as for the translation task with a single letter. Performance for the following passes decreases slightly.

Multi-headed resonator. Instead of running several passes of the resonator and explaining-away the result after each pass, we propose the *multi-headed resonator*. The multi-headed resonator explains several letters in parallel. It consists of several identical copies of the resonator that run in parallel and compete to explain parts of the input image. The same explaining-away procedure is utilized but after each iteration instead of at the end of the pass. Whenever one head has found and is close to converging to one of the letters, this letter is subtracted from the input and therefore

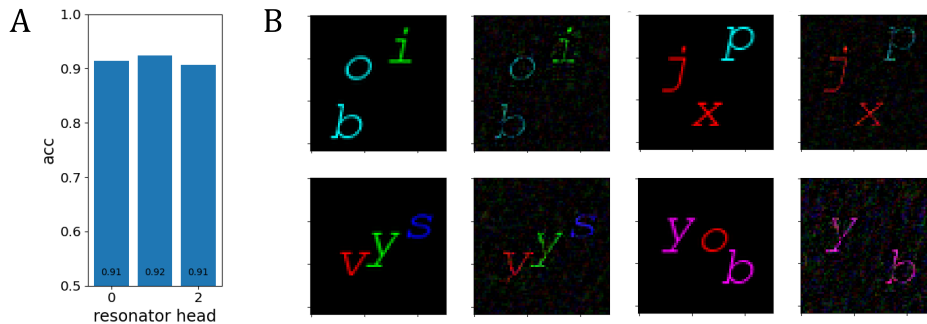


FIG. 8. Benchmarking of the multi-headed resonator network for the letter translation task with 3 random letters, 500 random samples. **A.** Letter classification accuracy for each of the 3 heads. **B.** Four random example input images and the reconstruction from the final resonator states. Bottom-right shows mistake example that misses the red ‘o’.

model version	accuracy (%)
full model	98.4
without noise	96.0
without aligned whitening	93.8
without ReLU ($k = 1, N = 30K$)	92.6
without ReLU ($k = 2, N = 10K$)	92.1

TABLE I. Testing of different model variants of the resonator on the letter translation task.

becomes invisible to the other heads. Fig. 8 shows the results for the 3-headed resonator solving the translation task with three letters.

Explaining away procedures. We explore explaining away both in the image space and in the latent (VSA) space. In the VSA space, the product of all resonator states (i.e. all factors bound together) is subtracted from the encoded input before it is sent to the next pass or used by the other heads. For explaining-away in the image space, the resonator network state is used to reconstruct the image. This image is then max normalized and all values below a threshold (0.1) are set to 0. The reconstruction image is rescaled and then subtracted from the input image to remove all correlation. The result is thresholded again to get rid of values below 0. The resulting residual image is then encoded into a VSA vector and used as input.

The subtraction in the latent VSA space is computationally cheaper as the image does not have to be reconstructed, but so far comes with a drop in performance (of 10-15%) as the states are less clean and additionally cannot fully explain away the input image due to the whitening. One could experiment with additional, stronger (higher k) cleanup with the non-whitened codebook for this purpose.

Ablation experiments. We test different variants of the resonator model to determine the importance of the algorithmic components, see Table I.

Details of hardware implementation

We implement a smaller model that solves a $28 \times 28 \times 3$ factorization task on Intel’s neuromorphic research chip Loihi [41]. The smaller version is implemented on the USB form factor system “Kapoho Bay” which features two Loihi chips with a total of 256 neuro cores in which a total of 262,144 neurons and up to 260 million synapses can be implemented. The embedded x86 processors are used for monitoring and sending input spikes.

By using phasors in a spiking network, operations of multiplication and addition of complex vectors become available on the hardware. Phasors can be implemented either with resonate and fire neurons or, by adding certain constraints, with common integrate and fire neurons [54]. In this work, we use integrate and fire neurons with a single spike per cycle of $T=16$ timesteps, which allows us to represent complex numbers of unit magnitude and discrete (4-bit) phase. Each complex component of a hyperdimensional vector is implemented on the hardware as a neuron.

The binding operation in FHRR is the Hadamard product (elementwise multiplication) between complex vectors. The multiplication of unit complex numbers is just the addition of their phases. We represent the phases of complex numbers as spike timing, and thus binding is a shift of spike times. To achieve the correct shift of spike-timing, we

Notation		Factors		Transforms	
$\hat{\mathbf{A}}$	Whitened codebook	$\mathbf{c} / \hat{\mathbf{C}}$	Color	$\hat{\Phi}, \hat{\Phi}_P, \hat{\Phi}_L, \mathbf{G}$	VSA codebooks
$\hat{\mathbf{a}}$	Factor estimate	\mathbf{h} / \mathbf{H}	Horizontal position	$\mathbf{L} (\Lambda)$	Log-polar transform (VSA space)
\mathbf{A}^\dagger	Complex conjugate transpose	\mathbf{v} / \mathbf{V}	Vertical position	$\mathbf{s} = \hat{\Phi}\mathbf{I}$	Input image
\mathbf{a}^*	Complex conjugate	\mathbf{r} / \mathbf{R}	Rotation	$\mathbf{D} = \hat{\Phi}_P\mathbf{P}$	Template images
$\mathbf{a} \odot \mathbf{b}$	Binding (Hadamard Product)	\mathbf{m} / \mathbf{M}	Scale factor	$\mathbf{D}_L = \Lambda\mathbf{D} = \hat{\Phi}_L\mathbf{L}\mathbf{P}$	Log-polar templates
$\mathbf{a} + \mathbf{b}$	Summation or superposition	$\mathbf{d} / \hat{\mathbf{D}} / \hat{\mathbf{D}}_L$	Centered template	$\mathbf{C} = \mathbf{G}\mathbf{B}$	Generative Colors
\mathbf{a}^{-1}	Inverse				
$\Re(a)$	Real part of complex number				

TABLE II. Notation and symbols reference

designed a 4-compartment neuron compatible with Loihi 1. The structure of this neuron is shown in Figure 5B and the mechanism is illustrated in Figure 5C.

Note that there are two versions of the binding circuit, one for binding and one for unbinding. Unbinding in FHR is elementwise multiplication with the complex conjugate (denoted by $*$ in the equations), i.e., phases are subtracted instead of added. In the binding circuit, the ‘aux’ compartment counts down from 0 to $-T$; in the unbinding circuit, the ‘aux’ compartment counts up from $-T$ to 0. This way, the timing of the spike arriving at the ‘trig’ compartment has the opposite effect on the timing of the ‘soma’ output spike. This works as modulo T addition of x is the same as modulo T subtraction of $T-x$.

After the binding module, spikes are sent through a cleanup module which performs a matrix multiplication with the auto-associative matrix, e.g., HH^\dagger . As described in Fig. 5, each spike through the clean-up matrix elicits a negative and positive current impulse. The impulse is delayed using Loihi’s synaptic delay settings, and the delay is based on the phase of the complex weight as described in [54]. This results in an approximation of sine-wave oscillations that occur in each LIF neuron’s membrane potential, which when summed together implement the complex dot-product.

To coordinate the timing of the network, there is a gate after the cleanup module. The gate module consists of an array of LIF neurons of length N that is connected in a 1:1 manner from the cleanup module to the binding module. The neurons are inhibited by default, and only allow spikes to relay when also depolarized by control input. The synaptic delays of the gate are adjusted to ensure that the binding module and the cleanup module remain synchronized. Further, the gate allows for the cleanup module to iterate for three cycles before forwarding spikes to the binding module. The gate also ensures that only 1 spike per cycle is routed to the binding module.

In order to reach better convergence, the cleanup module has a recurrent 1:1 connectivity, i.e., each neuron is connected back to itself with a delay of one cycle T . This leads to slower evolution of the resonator state over iterations, akin to the hysteresis procedure (11).

Because on the chip, fanout (the number of connections allowed to leave a neuron) is limited per core, we distributed neurons on several cores over the chip and pruned half of the synapses with the lowest weights from the cleanup matrix. The dense cleanup matrix is the most limiting component of the architecture. An alternative would be to split the cleanup matrix into its two components, reducing the number of synapses significantly in most cases. However, the layer connecting the two matrix multiplications cannot be represented with a spiking phasor with unit magnitude. Graded spikes on the next version of Loihi could be used to enable phasors with a magnitude.

Power measurements for the Loihi 1 chip were obtained remotely using NxSDK version 0.9.9 on the Nahuku32 board ncl-ghrd-01. The Loihi board is interfaced to a system with an Intel Xeon CPU E5-2670 @ 2.60GHz and 128GiB of RAM running Ubuntu 20.04.4 LTS. Intel Labs provided both software API and hardware. All probes, including the output probes, except the energy probes, were deactivated. Energy was averaged over 20 resonator iterations. Measurements for the CPU are obtained with Intel SoC Watch on a system with an Intel Core i9-7920X CPU @ 2.9GHz and 128GiB of RAM running Ubuntu 20.04 LTS. Simulations were run with Python 3.8.10 and NumPy 1.23.1. The process was constrained to use 12 threads since we found this to provide the best energy-delay-product measurement. The energy of the DRAM was not included. The latency and energy were averaged over 10000 iterations. Dynamic energy was measured by subtracting the static energy that is used when running the system without the load for the same amount of time. So, dynamic energy is the energy associated with the computation and excludes leakage energy.

DATA AVAILABILITY

Data sharing is not applicable to this article as no datasets were generated or analyzed during the current study. The synthetic images of letters can be recreated with the provided code.

CODE AVAILABILITY

Demo is available at: epaxon.github.io/Research/resonator_template.html. The source code will be made available upon publication.

ACKNOWLEDGMENTS

A.R. discloses support for the research of this work from Accenture Labs, the Swiss National Science Foundation (SNSF) [ELMA PZOO2 168183], and the University of Zurich postdoc grant [FK-21-136]. G.I. discloses support for the publication of this work from SNSF [SMALL 20CH21 186999]. F.T.S. discloses support for the research of this work from NIH [1R01EB026955-01]. We thank Intel Neuromorphic Computing Lab for providing access to the Loihi hardware and related software. The authors thank Elvin Hajizada for running the CPU power measurements.

REFERENCES

-
- [1] T. Poggio, V. Torre, and C. Koch, "Computational vision and regularization theory," *Readings in computer vision*, pp. 638–643, 1987.
 - [2] I. Yildirim, M. Belledonne, W. Freiwald, and J. Tenenbaum, "Efficient inverse graphics in biological face processing," *Science advances*, vol. 6, no. 10, p. eaax5979, 2020.
 - [3] C. Szegedy, W. Zaremba, I. Sutskever, J. Bruna, D. Erhan, I. Goodfellow, and R. Fergus, "Intriguing properties of neural networks," *arXiv preprint arXiv:1312.6199*, 2013.
 - [4] A. Madry, A. Makelov, L. Schmidt, D. Tsipras, and A. Vladu, "Towards deep learning models resistant to adversarial attacks," *arXiv preprint arXiv:1706.06083*, 2017.
 - [5] A. Nguyen, J. Yosinski, and J. Clune, "Deep neural networks are easily fooled: High confidence predictions for unrecognizable images," in *Proceedings of the IEEE conference on computer vision and pattern recognition*, pp. 427–436, 2015.
 - [6] A. Kurakin, I. J. Goodfellow, and S. Bengio, "Adversarial examples in the physical world," in *Artificial intelligence safety and security*, pp. 99–112, Chapman and Hall/CRC, 2018.
 - [7] D. M. MacKay, "Towards an information-flow model of human behaviour," *British Journal of Psychology*, vol. 47, no. 1, pp. 30–43, 1956.
 - [8] U. Neisser, *Cognitive psychology*. Appleton-Century-Crofts, 1966.
 - [9] A. Yuille and D. Kersten, "Vision as bayesian inference: analysis by synthesis?," *Trends in cognitive sciences*, vol. 10, no. 7, pp. 301–308, 2006.
 - [10] M. Davies, A. Wild, G. Orchard, Y. Sandamirskaya, G. A. F. Guerra, P. Joshi, P. Plank, and S. R. Risbud, "Advancing neuromorphic computing with loihi: A survey of results and outlook," *Proceedings of the IEEE*, pp. 1–24, 2021.
 - [11] P. A. Merolla, J. V. Arthur, R. Alvarez-Icaza, *et al.*, "A Million Spiking-neuron Integrated Circuit with a Scalable Communication Network and Interface," *Science*, vol. 345, no. 6197, pp. 668–673, 2014.
 - [12] S. Furber, F. Galluppi, S. Temple, and L. Plana, "The SpiNNaker project," *Proceedings of the IEEE*, vol. 102, pp. 652–665, May 2014.
 - [13] S. Moradi, N. Qiao, F. Stefanini, and G. Indiveri, "A scalable multicore architecture with heterogeneous memory structures for dynamic neuromorphic asynchronous processors (DYNAPs)," *Biomedical Circuits and Systems, IEEE Transactions on*, vol. 12, pp. 106–122, Feb. 2018.
 - [14] J. Pei, L. Deng, S. Song, M. Zhao, Y. Zhang, S. Wu, G. Wang, Z. Zou, Z. Wu, W. He, F. Chen, N. Deng, S. Wu, Y. Wang, Y. Wu, Z. Yang, C. Ma, G. Li, W. Han, H. Li, H. Wu, R. Zhao, Y. Xie, and L. Shi, "Towards artificial general intelligence with hybrid tianjic chip architecture," *Nature*, vol. 572, pp. 106–124, Aug. 2019.
 - [15] G. Indiveri and S.-C. Liu, "Memory and information processing in neuromorphic systems," *Proceedings of the IEEE*, vol. 103, no. 8, pp. 1379–1397, 2015.
 - [16] G. Gallego, T. Delbruck, G. M. Orchard, C. Bartolozzi, B. Tabak, A. Censi, S. Leutenegger, A. Davison, J. Conradt, K. Daniilidis, and D. Scaramuzza, "Event-based vision: A survey," *IEEE transactions on pattern analysis and machine intelligence*, vol. PP, jul 2020.
 - [17] C. von der Malsburg, "The correlation theory of brain function," Tech. Rep. 81-2, Max-Planck-Institute for Biophysical Chemistry, Göttingen, Germany, 1981.

- [18] C. Von der Malsburg, “Binding in models of perception and brain function,” *Current opinion in neurobiology*, vol. 5, no. 4, pp. 520–526, 1995.
- [19] D. E. Feldman, “The spike-timing dependence of plasticity,” *Neuron*, vol. 75, pp. 556–571, aug 2012.
- [20] J.-H. Jacobsen, J. Behrmann, R. Zemel, and M. Bethge, “Excessive invariance causes adversarial vulnerability,” *arXiv preprint arXiv:1811.00401*, 2018.
- [21] T. A. Plate, “Holographic Reduced Representations,” *IEEE Transactions on Neural Networks*, vol. 6, no. 3, pp. 623–641, 1995.
- [22] P. Kanerva, “Binary spatter-coding of ordered k-tuples,” in *Artificial neural networks —ICANN 96* (C. Malsburg, W. Seelen, J. C. Vorbrüggen, B. Sendhoff, G. Goos, J. Hartmanis, and J. Leeuwen, eds.), vol. 1112 of *Lecture notes in computer science*, pp. 869–873, Berlin, Heidelberg: Springer Berlin Heidelberg, 1996.
- [23] R. W. Gayler and R. Wales, “Connections, Binding, Unification and Analogical Promiscuity,” in *Advances in Analogy Research: Integration of Theory and Data from the Cognitive, Computational, and Neural Sciences*, pp. 1–11, 1998.
- [24] R. W. Gayler, “Vector Symbolic Architectures Answer Jackendoff’s Challenges for Cognitive Neuroscience,” in *Joint International Conference on Cognitive Science (ICCS/ASCS)*, pp. 133–138, 2003.
- [25] P. Kanerva, “Hyperdimensional computing: An introduction to computing in distributed representation with high-dimensional random vectors,” *Cognitive computation*, vol. 1, pp. 139–159, jun 2009.
- [26] D. Kleyko, M. Davies, E. P. Frady, *et al.*, “Vector Symbolic Architectures as a Computing Framework for Nanoscale Hardware,” *arXiv:2106.05268*, pp. 1–28, 2021.
- [27] E. Frady, D. Kleyko, C. Kymn, B. Olshausen, and F. Sommer, “Computing on functions using randomized vector representations,” *arXiv preprint arXiv:2109.03429*, 2021.
- [28] E. P. Frady, S. J. Kent, B. A. Olshausen, and F. T. Sommer, “Resonator networks, 1: An efficient solution for factoring high-dimensional, distributed representations of data structures,” *Neural Computation*, pp. 1–21, oct 2020.
- [29] S. J. Kent, E. P. Frady, F. T. Sommer, and B. A. Olshausen, “Resonator networks, 2: Factorization performance and capacity compared to optimization-based methods,” *Neural Computation*, vol. 32, pp. 2332–2388, dec 2020.
- [30] W. Pitts and W. S. McCulloch, “How we know universals the perception of auditory and visual forms,” *The Bulletin of mathematical biophysics*, vol. 9, no. 3, pp. 127–147, 1947.
- [31] G. F. Hinton, “A parallel computation that assigns canonical object-based frames of reference,” in *Proceedings of the 7th international joint conference on Artificial intelligence-Volume 2*, pp. 683–685, 1981.
- [32] B. A. Olshausen, C. H. Anderson, and D. C. Van Essen, “A neurobiological model of visual attention and invariant pattern recognition based on dynamic routing of information,” *Journal of Neuroscience*, vol. 13, no. 11, pp. 4700–4719, 1993.
- [33] D. W. Arathorn, *Map-seeking circuits in visual cognition: A computational mechanism for biological and machine vision*. Stanford University Press, 2002.
- [34] D. Arathorn, “Computation in the higher visual cortices: Map-seeking circuit theory and application to machine vision,” in *33rd Applied Imagery Pattern Recognition Workshop (AIPR’04)*, pp. 73–78, IEEE, 2004.
- [35] J. Tenenbaum and W. Freeman, “Separating style and content,” *Advances in neural information processing systems*, vol. 9, 1996.
- [36] W. T. Freeman and J. B. Tenenbaum, “Learning bilinear models for two-factor problems in vision,” in *Proceedings of IEEE Computer Society Conference on Computer Vision and Pattern Recognition*, pp. 554–560, IEEE, 1997.
- [37] M. A. O. Vasilescu and D. Terzopoulos, “Multilinear analysis of image ensembles: Tensorfaces,” in *European conference on computer vision*, pp. 447–460, Springer, 2002.
- [38] B. A. Olshausen, C. Cadieu, J. Culpepper, and D. K. Warland, “Bilinear models of natural images,” in *Human Vision and Electronic Imaging XII*, vol. 6492, pp. 67–76, SPIE, 2007.
- [39] H. Y. Chau, F. Qiu, Y. Chen, and B. Olshausen, “Disentangling images with lie group transformations and sparse coding,” *arXiv preprint arXiv:2012.12071*, 2020.
- [40] E. P. Frady, D. Kleyko, and F. Sommer, “Variable binding for sparse distributed representations: Theory and applications,” *arXiv preprint arXiv:2009.06734*, 2020.
- [41] M. Davies, N. Srinivasa, T.-H. Lin, G. Chinya, Y. Cao, S. H. Choday, G. Dimou, P. Joshi, N. Imam, S. Jain, *et al.*, “Loihi: A neuromorphic manycore processor with on-chip learning,” *IEEE Micro*, vol. 38, no. 1, pp. 82–99, 2018.
- [42] P. Frady, P. Kanerva, and F. Sommer, “A framework for linking computations and rhythm-based timing patterns in neural firing, such as phase precession in hippocampal place cells,” *CCN*, 2019.
- [43] B. Komer, T. Stewart, A. Voelker, and C. Eliasmith, “A neural representation of continuous space using fractional binding,” in *Annual Meeting of the Cognitive Science Society (CogSci)*, pp. 2038–2043, Cognitive Science Society, 2019.
- [44] D. Kleyko, D. A. Rachkovskij, E. Osipov, and A. Rahimi, “A Survey on Hyperdimensional Computing aka Vector Symbolic Architectures, Part I: Models and Data Transformations,” *arXiv:2111.06077*, pp. 1–27, 2021.
- [45] D. Kleyko, D. A. Rachkovskij, E. Osipov, and A. Rahimi, “A Survey on Hyperdimensional Computing aka Vector Symbolic Architectures, Part II: Applications, Cognitive Models, and Challenges,” *arXiv:2112.15424*, pp. 1–36, 2021.

- [46] T. A. Plate, *Distributed Representations and Nested Compositional Structure*. University of Toronto, PhD Thesis, 1994.
- [47] A. Rahimi and B. Recht, “Random features for large-scale kernel machines,” in *Advances in Neural Information Processing Systems (NIPS)*, vol. 20, pp. 1–8, 2007.
- [48] E. P. Frady, D. Kleyko, and F. T. Sommer, “A theory of sequence indexing and working memory in recurrent neural networks.,” *Neural Computation*, vol. 30, pp. 1449–1513, apr 2018.
- [49] J. B. Tenenbaum and W. T. Freeman, “Separating Style and Content with Bilinear Models,” *Neural Computation*, vol. 12, no. 6, pp. 1247–1283, 2000.
- [50] Y. W. Teh, M. Welling, S. Osindero, and G. E. Hinton, “Energy-based models for sparse overcomplete representations,” *Journal of Machine Learning Research*, vol. 4, no. Dec, pp. 1235–1260, 2003.
- [51] T. Kohonen, “An adaptive associative memory principle,” *IEEE Transactions on Computers*, vol. 100, no. 4, pp. 444–445, 1974.
- [52] R. L. Burden, J. D. Faires, and A. M. Burden, *Numerical analysis*. Cengage learning, 2015.
- [53] D. J. Felleman and D. C. Van Essen, “Distributed hierarchical processing in the primate cerebral cortex.,” *Cerebral cortex (New York, NY: 1991)*, vol. 1, no. 1, pp. 1–47, 1991.
- [54] E. P. Frady and F. T. Sommer, “Robust computation with rhythmic spike patterns.,” *Proceedings of the National Academy of Sciences of the United States of America*, vol. 116, pp. 18050–18059, sep 2019.
- [55] A. Renner, L. Supic, A. Danielescu, G. Indiveri, F. T. Sommer, E. P. Frady, and Y. Sandamirskaya, “Neuromorphic visual odometry with resonator networks,” *arXiv preprint arXiv:2209.02000*, 2022.
- [56] D. Casasent and D. Psaltis, “Position, rotation, and scale invariant optical correlation,” *Applied optics*, vol. 15, no. 7, pp. 1795–1799, 1976.
- [57] Q.-s. Chen, M. Defrise, and F. Deconinck, “Symmetric phase-only matched filtering of fourier-mellin transforms for image registration and recognition,” *IEEE Transactions on pattern analysis and machine intelligence*, vol. 16, no. 12, pp. 1156–1168, 1994.
- [58] B. S. Reddy and B. N. Chatterji, “An fft-based technique for translation, rotation, and scale-invariant image registration,” *IEEE transactions on image processing*, vol. 5, no. 8, pp. 1266–1271, 1996.
- [59] D. H. Ballard, “Cortical connections and parallel processing: Structure and function,” *Behavioral and brain sciences*, vol. 9, no. 1, pp. 67–90, 1986.
- [60] E. Bienenstock and C. von der Malsburg, “A neural network for invariant pattern recognition,” *Europhysics Letters*, vol. 4, no. 1, p. 121, 1987.
- [61] K. Fukushima and S. Miyake, “Neocognitron: A self-organizing neural network model for a mechanism of visual pattern recognition,” in *Competition and cooperation in neural nets*, pp. 267–285, Springer, 1982.
- [62] A. Azulay and Y. Weiss, “Why do deep convolutional networks generalize so poorly to small image transformations?,” *arXiv preprint arXiv:1805.12177*, 2018.
- [63] E. P. Frady, S. Kent, Q. Tran, P. Kanerva, B. A. Olshausen, and F. T. Sommer, “Learning and generalization of compositional representations of visual scenes,” 2023.
- [64] R. Geirhos, J.-H. Jacobsen, C. Michaelis, R. Zemel, W. Brendel, M. Bethge, and F. A. Wichmann, “Shortcut learning in deep neural networks,” *Nature Machine Intelligence*, vol. 2, no. 11, pp. 665–673, 2020.
- [65] M. A. Alcorn, Q. Li, Z. Gong, C. Wang, L. Mai, W.-S. Ku, and A. Nguyen, “Strike (with) a pose: Neural networks are easily fooled by strange poses of familiar objects,” in *Proceedings of the IEEE/CVF conference on computer vision and pattern recognition*, pp. 4845–4854, 2019.
- [66] V. Biscione and J. Bowers, “Learning translation invariance in cnns,” *arXiv preprint arXiv:2011.11757*, 2020.
- [67] C. R. Vogel, D. W. Arathorn, A. Roorda, and A. Parker, “Retinal motion estimation in adaptive optics scanning laser ophthalmoscopy,” *Optics express*, vol. 14, no. 2, pp. 487–497, 2006.
- [68] S. Chaudhuri, D. Ritchie, J. Wu, K. Xu, and H. Zhang, “Learning generative models of 3d structures,” in *Computer Graphics Forum*, vol. 39, pp. 643–666, Wiley Online Library, 2020.
- [69] J. Huang and K. Murphy, “Efficient inference in occlusion-aware generative models of images,” *arXiv preprint arXiv:1511.06362*, 2015.
- [70] D. Kleyko, D. A. Rachkovskij, E. Osipov, and A. Rahimi, “A survey on hyperdimensional computing aka vector symbolic architectures, part II: applications, cognitive models, and challenges,” *CoRR*, vol. abs/2112.15424, 2021.
- [71] A. Renner, Y. Sandamirskaya, F. T. Sommer, and E. P. Frady, “Sparse vector binding on spiking neuromorphic hardware using synaptic delays,” in *International Conference on Neuromorphic Systems (ICONS 2022)*, ACM, 2022.
- [72] C. Geisler, D. Robbe, M. Zugaro, A. Sirota, and G. Buzsáki, “Hippocampal place cell assemblies are speed-controlled oscillators.,” *Proceedings of the National Academy of Sciences of the United States of America*, vol. 104, pp. 8149–8154, may 2007.
- [73] N. Burgess, C. Barry, and J. O’Keefe, “An oscillatory interference model of grid cell firing.,” *Hippocampus*, vol. 17, no. 9, pp. 801–812, 2007.